RSC Advances

PAPER

View Article Online
View Journal | View Issue

Cite this: *RSC Adv.*, 2025, **15**, 42229

Impact on increasing the bent angle in nickel dibenzoporphyrin(2.1.2.1) bows. Evaluation of structural and molecular features from computations

Margot Paco-Chipana[a] and Alvaro Muñoz-Castro *[b]

Non-planar porphyrin motifs enable particular characteristics relevant for a wide range of applications. We explored (through computations) the features of increasing the bend in the more flexible dibenzoporphyrin (2.1.2.1) core. We decreased the bridge length from the recently reported butadiyne-bridged dibenzoporphyrin(2.1.2.1), and its nickel counterpart. Our results highlighted the flexibility of the dibenzoporphyrin(2.1.2.1) core, which could bend from 122.4° to 103.2° involving a strain energy of <3.4 kcal mol^{-1}, and of 9.1 kcal mol^{-1} from 116.0° to 97.3° upon incorporating the central nickel atom. For further bent angles, destabilization of the dibenzoporphyrin(2.1.2.1) core increased to 23.7 and 38.5 kcal mol^{-1}, respectively. This structural control modified the HOMO–LUMO gap and optical absorption patterns, and highlighted an increase in the Lewis acid capabilities of the resulting π-hole site perpendicular to the N4 molecular plane, in comparison with the parent nickel porphyrin, evaluated *via* calculated fluoride ion affinity. In addition, the induced magnetic field had a deshielding region ascribed to N4- and NiN4-motifs, which was retained within the bent cavity. These observations indicate that controlled bending of N4 is a useful synthetic strategy to tune the capabilities of porphyrin- and metalloporphyrin-like species.

Received 2nd October 2025
Accepted 15th October 2025

DOI: 10.1039/d5ra07496g

rsc.li/rsc-advances

Introduction

Non-planar porphyrin molecules exhibit intriguing features provided by their curved and strained structural backbones in comparison with planar motifs.[1–4] These features lead to particular characteristics desired for applications ranging from biological models to functional electronic devices as sensors, optoelectronic, and photovoltaic species.[5–10] The deviation from planarity can be induced and controlled by introducing the strain of the central motif, like in corannulene[11] or tetraphenylene.[12,13] This planarity deviation can be "tuned" by a delicate choice of the central structural core and the subsequent variation of peripheral substituents, among other approaches,[14–16] resulting in a bowl- or saddle-shaped motif. The use of sterically demanding exo-substituents or cofacial aggregation[17,18] has been employed to achieve an unprecedented perfectly planar corannulene structure. The use of a bridge connecting two different sites within the central core enables the introduction of a concave face in bent pyrenes.[19,20]

Early strategies to introduce non-planarity in porphyrin macrocyles have been developed by incorporating a bridging "bow limb" at the β-positions of the pyrrolic units,[21,22] serving to stretch the planar porphyrin(1.1.1.1). Such an approach serves to increase the versatility of porphyrins and metalloporphyrins, resulting in interesting building blocks with tuned characteristics.[23–27] Despite these achievements, the rigid characteristics of the porphyrin reduce the scope of planarity loss of the central structural core, where the use of inherently bent motifs serves to provide a more efficient curved situation.

In this respect, the work by Xue and coworkers explored the use of bent porphyrin structural cores given by the extended dibenzoporphyrin(2.1.2.1).[28–38] This enabled an increase in the non-planarity of the coordinating N4-site,[39] with interesting performance in electrocatalytic hydrogen evolution reaction (HER) activity for fused arrays. Furthermore, these authors conceived a mixed approach involving a bridging "bow limb" with the bent dibenzoporphyrin(2.1.2.1) core by using a butadiyne-bridge connected to exo-aryl rings within the dibenzoporphyrin(2.1.2.1) structure. This led to an increased strain, inducing a larger bowl-shaped deformation from planarity.[40]

We set out to explore the bent characteristics of the metal-free and nickel-incorporated butadiyne-bridged dibenzoporphyrin(2.1.2.1) (**Por** and **PorNi**, respectively),[40] and

[a]*Doctorado en Biología Computacional, Facultad de Ingeniería, Universidad San Sebastián, Bellavista 7, Santiago, Chile*
[b]*Facultad de Ingeniería, Universidad San Sebastián, Bellavista 7, Santiago, Chile. E-mail: alvaro.munozc@uss.cl*

further consequences of a more bent structure, by evaluating shorter-bridge situations involving acetylene- and directly-bridged exo-aryl rings. Our results are given in terms of the different energy contributions to the energy difference as the porphyrin bends, the resulting patterns of optical absorption, the induced magnetic field, and the variations at the N4-site. From such observations, further understanding of the capabilities in bending N4-motifs based on the bridged dibenzoporphyrin(2.1.2.1) core was evaluated, denoting the capabilities to tune different molecular characteristics.

Computational details

Geometry optimizations and subsequent calculations were performed at the density functional theory (DFT) level employing the ADF code.[41,42] We used the all-electron triple-ζ Slater basis set augmented with double polarization functions (STO-TZ2P) and the hybrid functional of Perdew, Burke, and Ernzerhof provided by Ernzerhof–Scuseria and Adamo–Barone (PBE0).[43–45] London dispersion correction to DFT was taken into account by the pairwise method of Grimme (DFT-D3).[46] Open-shell structures were treated under the unrestricted Kohn–Sham regime. Vibrational analysis was carried out to determine the minima character of the most favorable conformation, and the transition state nature of the involved transition states, as a first-order saddle point in the potential energy surface (one negative frequency). Time-dependent DFT (TD-DFT) calculations were carried out to simulate the optical UV-Vis spectrum for the studied series using all-electron TZ2P basis sets and the statistical averaging of different orbital-dependent model potentials (SAOP), which incorporate important features of the exact potential in the molecular and asymptotic regions, employed previously for metalloporphyrins and tetrapyrroles.[47] To evaluate the magnetic response or induced field ($\mathbf{B}^{ind}$), upon an external magnetic field ($\mathbf{B}^{ext}$), a two-dimensional representation of the nucleus independent chemical shielding (NICS) tensor (σ_{ij}) was obtained, where $\mathbf{B}_i^{ind} = -\sigma_{ij}\mathbf{B}_j^{ext}$.[48–52] For convenience, the i and j suffixes correspond to the x-, y-, and z-axes of the molecule-fixed Cartesian system ($i,j = x,y,z$). $\mathbf{B}^{ind}$ is given in ppm in relation to $\mathbf{B}^{ext}$.

Results and discussion

The metal-free and nickel butadiyne-bridged dibenzoporphyrin(2.1.2.1), noted by **Por** and **PorNi**, respectively, are schematically given in Scheme 1. The optimized structures are given in Fig. 1, which denotes calculated distances between *ipso*-carbon from *meso*-phenyl units of 7.588 and 7.473 Å, which are in good agreement with the structurally characterized distances of 7.54 and 7.46 Å.[40] For the free base, **Por**, the experimental distance from N and N–H to a central centroid was 2.007 and 2.179 Å, which has been calculated to be 1.980 and 2.177 Å.[40] Upon inclusion of the Ni metal center in **PorNi**, experimental N–Ni distances amounted to 1.892 and 1.903 Å,[40] which was calculated at 1.901 and 1.908 Å, respectively.

The angle between both *meso*-carbons and the N4-centroid was 123.5° and 116.2° for **Por** and **PorNi**, respectively, which was calculated to be 122.1° and 116.0°, showing a more bent structure upon inclusion of the Ni metal center. For the sake of simplicity, hereafter the **Por** and **PorNi** species are denoted as **1** and **1Ni**.

We wished to evaluate the energy related to the induced deformation of the dibenzoporphyrin(2.1.2.1) core. We provided the energy difference between the unsubstituted dibenzoporphyrin(2.1.2.1) (**0** and **0Ni**) and its resulting structure within the **1** and **1Ni** species. To offer a direct comparison, the bridging biphenyl butadiyne (-Ph–CCCC–Ph-), acetylene (-Ph–CC–Ph-) and biphenyl (-Ph-Ph-) motifs were removed and replaced by –H, for **1**/**1Ni**, **2**/**2Ni** and **3**/**3Ni**, respectively. This enabled retention of their structures obtained in the overall structures (**1**/**1Ni**, **2**/**2Ni** and **3**/**3Ni**), thereby leaving the distorted dibenzoporphyrin(2.1.2.1) for a direct comparison. Results indicated a deformation energy of 0.9 and 2.0 kcal mol^{-1} upon inclusion of the butadiyne-bridged structure, which was bent to achieve its structure in **1** and **1Ni**. Such values exposed the flexibility of the dibenzoporphyrin(2.1.2.1) core, which required a small amount of energy to increase its bowl-shape structure as given by the angle between both *meso*-carbons and the N4-centroid.

Furthermore, by replacing the butadiyne-bridge with an acetylene-based bridge, denoted by **2** and **2Ni**, the distances between *ipso*-carbons from the *meso*-phenyl units in the free

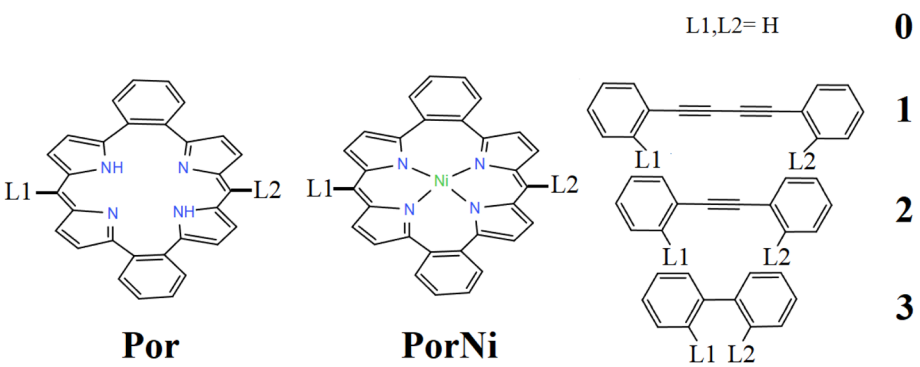

Scheme 1 **Por** and **PorNi** cores, linked by L1 and L2 connection points for the giver bridges for **1**, **2** and **3**, and by H in **0**.

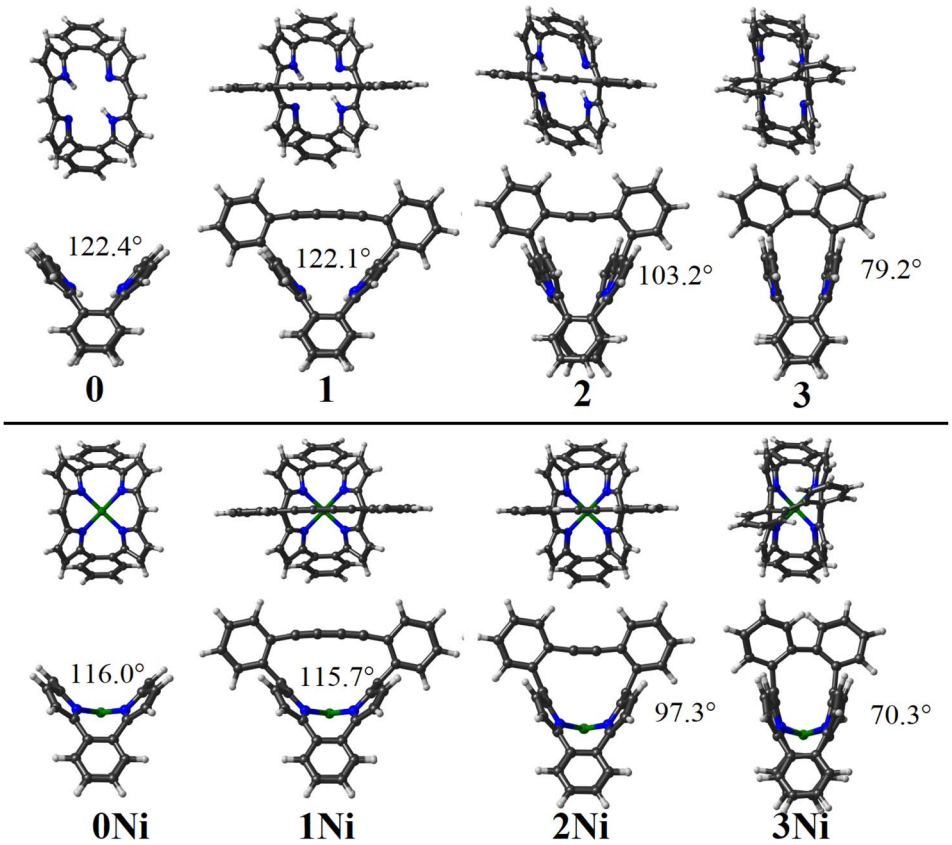

Fig. 1 Calculated structures for the studied series, denoting the bent angle of the dibenzoporphyrin(2.1.2.1) motif, given from upper and side views.

base (**2**) decreased to 5.801 and 5.817 Å in the nickel-incorporated counterpart (**2Ni**). This led to a narrower *meso*-carbons and N4-centroid angle of 103.2° and 97.3°, for **2** and **2Ni**, respectively. This denoted a larger planarity deviation for the dibenzoporphyrin(2.1.2.1) core, which interestingly involved only a small destabilization of 3.4 kcal mol^{-1} for the freebase (**2**), which increased to 9.1 kcal mol^{-1} after Ni-coordination in **2Ni**. This denoted that the metal-coordinated porphyrin core introduced a larger strain or rigidity for bent processes, serving to control the degree of deformation for the porphyrin core.

Removal of the acetylene-bridge, leaving both *meso*-phenyl rings to be directly connected, similar to a *para*-bisphenyl motif, resulted in shorter distances between *ipso*-carbons from the *meso*-phenyl units of 3.584 and 3.618 Å, for **3** and **3Ni**, resulting in a very narrow angle between *meso*-carbons and the N4-centroid of 79.2° and 70.3°. Such an exaggerated induced bending of the dibenzoporphyrin(2.1.2.1) core involved deformation energies of 23.7 and 38.5 kcal mol^{-1}, indicating that such structures were more destabilized compared with the above-discussed scenarios (**1**, **1Ni**, **2**, and **2Ni**), making them challenging synthetic targets.

The calculated gap between frontier orbitals (HOMO–LUMO gap) ranged from 3.28 to 2.61 eV in decreasing **0** > **1** > **2** > **3** order (Fig. 2), denoting the role of reducing the angle between *meso*-carbons and N4-centroid angle, in frontier orbitals. For the nickel counterparts, the variation in the HOMO–LUMO gap was smaller, ranging from 3.00 to 2.75 eV, and decreased in the order **0Ni** > **1Ni** > **2Ni** > **3Ni**. Hence, the inclusion of the metal center hampered stronger variations in the frontier orbital gap. In the series, HOMO−1 and HOMO were of π-dibenzoporphyrin(2.1.2.1) character (Fig. S1); LUMO and LUMO+1 were of π*-dibenzoporphyrin(2.1.2.1) character. For the bridged species, LUMO+2 remained close to the frontier orbitals formed by bridge-based orbitals, which were destabilized from **1** to **3**, and from **1Ni** to **3Ni**.

We wished to evaluate the variation of the N4–Ni coordination from **0Ni** to **3Ni**. The interaction energy (ΔE_{int}) leading to the Ni coordination into the N4 cavity was calculated in terms of the Ni^{2+}/ligand^{2-} fragmentation within the energy decomposition analysis.[53–55] This resulted in a sizable stabilization of −906.1 kcal mol^{-1} for **0Ni**, which decreased to −901.4, −897.7, and −887.6 for **1Ni**, **2Ni** and **3Ni**, respectively (Table 1). Thus, despite the increasing deviation from planarity, the N4-cavity from the dibenzoporphyrin(2.1.2.1) core could retain a sizable Ni-coordination, which decreased stepwise according to the bent angle from 116.2° to 70.3°, with a destabilizing energy difference of 18.4 kcal mol^{-1} between **0Ni** and **3Ni**. The respective calculated bond dissociation energy (BDE) followed

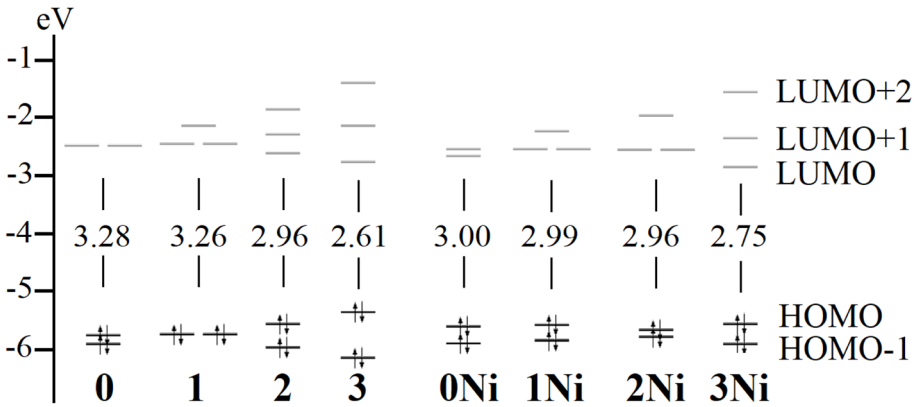

Fig. 2 Calculated frontier orbitals and the respective HOMO–LUMO gap.

a similar trend to the discussed interaction energy, denoting a decrease from **0Ni** to **3Ni** (Table 1).

Moreover, within the framework of energy decomposition analysis[53–55] provided by the Ziegler–Rauk energy decomposition scheme,[56] the interaction energy (ΔE_{int}) can be decomposed in several meaningful terms,[53–55] given by:

$$\Delta E_{int} = \Delta E_{Pauli} + \Delta E_{elstat} + \Delta E_{orb} + \Delta E_{disp}$$

In this sense, the decrease in the interaction energy in the N4–Ni coordination from **0Ni** to **3Ni** involved contributions from the destabilizing Pauli repulsion accounting for the steric hindrance effects (ΔE_{Pauli}), the variation in the stabilizing electrostatic character of the interaction (ΔE_{elstat}), and the stabilizing orbital character (ΔE_{orb}).[42] In addition, the contribution from London interactions (ΔE_{disp}) was accounted for by the pairwise correction from Grimme (D3).[57,58]

Interestingly, the stabilizing orbital character (ΔE_{orb}) of the interaction varied to a lesser extent from −521.7 to −533.0 kcal mol^{-1}, about −11 kcal mol^{-1}, despite the marked decrease in the bent angle from **0Ni** to **3Ni** (116.2° to 70.3°), thus retaining a similar coordination environment. The electrostatic character of the interaction (ΔE_{elstat}) varied from −668.2 to −649.6 kcal mol^{-1}, denoting a decreasing variation of ∼19 kcal mol^{-1}. The London interaction character (ΔE_{disp}) remained similar along with the series from **0Ni** to **3Ni**, with a variation of <0.3 kcal mol^{-1}. The Pauli repulsion (ΔE_{Pauli}) varied by 11.4 kcal mol^{-1} along with the group, showing a more sterically demanding coordination site in the most bent structure, namely **3Ni**. From these contributions, the energy difference associated with the nickel coordination was primarily due to a slight increase in the Pauli repulsion and a decrease in the stabilizing electrostatic character, which overcame the slightly more stabilizing orbital interaction variation, resulting in an overall destabilization as the dibenzoporphyrin(2.1.2.1) core bends.

Furthermore, the electrostatic potential at the van der Waals surface (Fig. 3) is a valuable tool in locating reactive sites within the resulting molecular structure. This is given by the formation of regions displaying a maximum in the surface electrostatic potential ($V_{S,max}$). These are noted as σ-holes in clusters[59,60] and as π-holes in metalloporphyrins,[61] accounting for the capabilities of Lewis acidic regions[62] leading to reactivity at the metal site. For nickel porphyrin, the π-hole site perpendicular to the N4 molecular plane[39] showed a slight negative region in the range of −10.2 kcal mol^{-1} for the unsubstituted nickel porphyrin (NiN4) and of −2.7 kcal mol^{-1} for the nickel tetra(4-bromo-2,6-difluorophenyl) porphyrin (Nippy).[61] Such features are in line with the observed nucleophilic character in square planar d^8 complexes (as stated previously[61,63,64]) and denoted as electrophilic–nucleophilic dualism at such π-hole sites.[65] For **0Ni**, the electrostatic potential above the nickel metal center was −9.5 kcal mol^{-1}, which increased to −10.3 kcal mol^{-1} in **1Ni**. Upon reducing the angle between both *meso*-carbons and the N4-centroid to 116.2° in **2Ni** and to 70.3° in **3Ni**, the respective electrostatic potential amounted to −11.1 and −11.2 kcal mol^{-1}.

Table 1 Energy decomposition analysis for the Ni^{2+}/ligand^{2-} fragmentation for the **0Ni** to **3Ni** series. In addition, related bond dissociation energies (BDEs) are provided. Values are in kcal mol^{-1}

	0Ni		1Ni		2Ni		3Ni	
ΔE_{Pauli}	289.7		285.3		294.42		301.04	
ΔE_{elstat}	−668.2	55.9%	−652.6	55.0%	−653.8	54.8%	−649.6	54.6%
ΔE_{orb}	−521.7	43.6%	−527.8	44.5%	−532.1	44.6%	−533.0	44.8%
ΔE_{disp}	−5.8	0.5%	−6.3	0.5%	−6.2	0.5%	−6.1	0.5%
ΔE_{int}	−906.1		−901.4		−897.7		−887.6	
BDE	850.2		846.3		835.5		815.2	

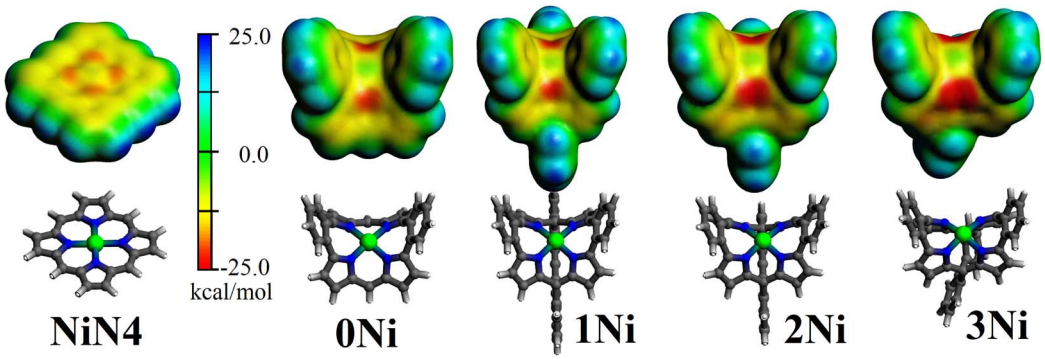

Fig. 3 Electrostatic potential at the van der Waals surface (isosurface = 0.001 a.u.) for the **0Ni**, **1Ni**, **2Ni** and **3Ni** series. In addition, the unsubstituted nickel porphyrin (NiN4) is included.

To evaluate the characteristics of the π-hole site, we calculated the fluoride ion affinity (FIA) introduced by Bartlett.[66,67] This is obtained as the negative of the enthalpy of the reaction of the π-hole with a fluoride ion in the gas phase, $FIA^{direct} = -\Delta H$.[68] Such an approach serves to classify the strength of the interaction in comparison with prototypical Lewis acids, provided by BF_3, $B(CF_3)_3$, and $B(C_6F_5)_3$ species.[69–72]

The calculated FIA for BF_3 was 349.7 kJ mol^{-1}, increasing to 441.1 kJ mol^{-1} for $B(C_6F_5)_3$, and to 554.7 kJ mol^{-1} for $B(CF_3)_3$, which are in line with the reported values of 342, 452 kJ mol^{-1} and 556 kJ mol^{-1}, respectively.[66,73] For the planar nickel porphyrin ($NiN_4C_{20}H_{14}$), the calculated FIA was 73.2 kJ mol^{-1}, denoting weaker Lewis acid capabilities in comparison with BF_3, $B(CF_3)_3$ and $B(C_6F_5)_3$ species. Interestingly, in the unsubstituted nickel dibenzoporphyrin(2.1.2.1) (**0Ni**), the calculated FIA increased to 136.1 kJ mol^{-1}, serving as a non-planar coordinating backbone modifying the characteristics of related planar metalloporphyrins. Upon inclusion of the butadiyne-bridge in the nickel dibenzoporphyrin(2.1.2.1) framework (**1Ni**), the calculated FIA increased further to 140.9, varying to 139.1 in **2Ni**, and to 149.7 kJ mol^{-1} for **3Ni**. These data suggested a mild Lewis acid capability for the resulting bent nickel dibenzoporphyrin(2.1.2.1).

We wished to evaluate the impact of shortening the connecting bridge from the studied series on the optical absorption pattern. Hence, TD-DFT calculations were carried out. For **1** and **1Ni**, the first main absorption peak appeared at 431 and 534 nm (noted as **Por** and **PorNi**, respectively, in[40]), denoting a broad shape owing to the overlap of different signals. The calculated absorption bands appeared at 468 and 512 nm for **1** and **1Ni**, respectively, within the method's error. Additionally, for **1** and **1Ni**, smaller secondary bands were observed at 407 and 481 nm, respectively, which were expected to remain overlapped in the experimental characterization. In the **0** to **3** series, the first peak remained at a similar energy (468, 468, 471, and 467 nm), of π → π*-dibenzoporphyrin(2.1.2.1) character, whereas the secondary peak appearing in **1** to **3** varied as 407, 366 and 359 owing to a π-dibenzoporphyrin(2.1.2.1) →π*-bridge character. From **0Ni** to **3Ni**, the first peak varied as 507, 512, 517, and 486 nm, respectively, retaining a π → π*-dibenzoporphyrin(2.1.2.1) character, whereas the secondary peak varied as 407, 351, and 284 nm, of π-dibenzoporphyrin(2.1.2.1) →π*-bridge character. Hence, the secondary peak was affected more by the involved bridge motif (Fig. 4).

Finally, to gain insights into the effect of introducing the different rings in the studied species, the induced magnetic field was evaluated.[52,74] This evaluation was in terms of NICS accounting for the orientationally averaged behavior owing to the constant molecular tumbling in solution, and under a specific orientation perpendicular to the N4-ring plane provided by $\mathbf{B}_z^{ind}$. According to the NICS contour plots (Fig. 5), for **0**, a central deshielding region (∼5.0 ppm) was located at the N4-ring, which decreased for **1** and **2**, and increased to ∼5.0 ppm at **3**. For $\mathbf{B}_z^{ind}$, the central deshielding region was enhanced with values > 10.0 ppm, which was retained at the N4 bent from **1** to **3** (which faced the shielding contribution from the bridging motif). For the nickel counterparts, the central deshielding region was enhanced (as seen from NICS contour plots), facing the shielding region from the bridge, denoting that such a deshielding region was contained within the bent region. For $\mathbf{B}_z^{ind}$, such observations were enhanced, indicating an increase in the deshielding region contained within the N4-cavity.

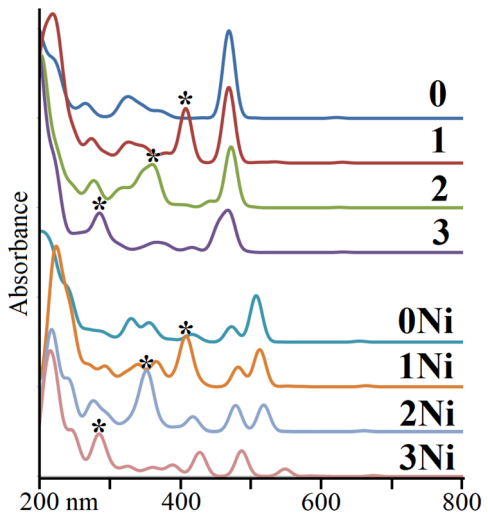

Fig. 4 Calculated UV–Vis patterns for **0** to **3**, and **0Ni** to **3Ni** series. The secondary peak is denoted by *.

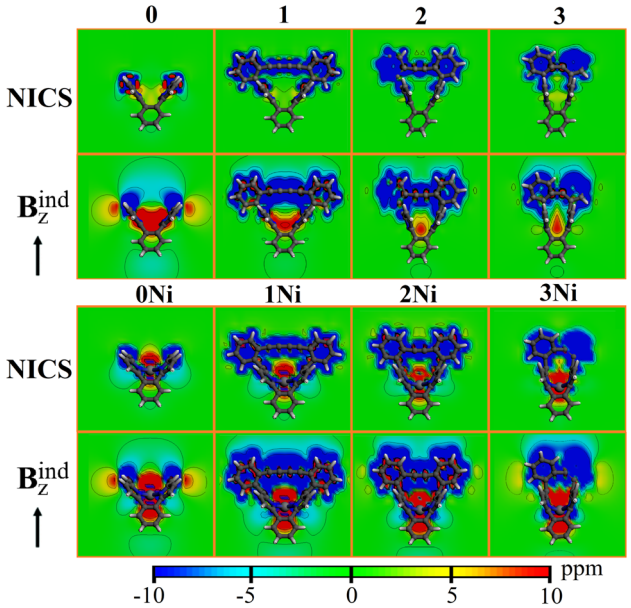

Fig. 5 Contour plots of NICS and B_z^{ext} for the studied species.

Conclusions

Variation in the structural features in porphyrin- and metalloporphyrin-like species based on the bridged dibenzoporphyrin(2.1.2.1) motif was studied. The flexibility of the N4-core could be bent from 122.4° to 103.2°, and involved a strain energy of <3.4 kcal mol^{-1}, and of 9.1 kcal mol^{-1} from 116.0° to 97.3° upon incorporation of the central nickel atom. Hence, the dibenzoporphyrin(2.1.2.1) core could be useful for further exploration of non-planar N4-motifs towards achieving tuned capabilities. Structural control of the bent angle could modify the HOMO–LUMO gap, and the optical absorption profiles could be determined. An increase in the Lewis acid capabilities of the resulting π-hole site perpendicular to the N4 molecular plane, in comparison with the pristine nickel porphyrin ring, was evaluated *via* FIA. Induced magnetic field analysis revealed a deshielding region to be retained within the bent cavity from N4- and NiN4-motifs in the bridged dibenzoporphyrin(2.1.2.1) species. These observations suggest controlled bending of N4 to be a useful synthetic strategy to tune the capabilities of porphyrin- and metalloporphyrin-like species.

Conflicts of interest

There are no conflicts to declare.

Data availability

The data supporting the conclusions reached from our study have been included as part of the supplementary information (SI). Supplementary information is available. See DOI: **https://doi.org/10.1039/d5ra07496g**.

Acknowledgements

M. P.-C. acknowledges a doctoral scholarship from Vicerrectoría de Investigación y Doctorados, Universidad San Sebastián. This work was supported by ANID FONDECYT REGULAR 1221676. The authors thank the financial support from USS-FIN-25-OVIN-13 from Vicerrectoría de Investigación y Doctorados, Universidad San Sebastián.

References

1 G. Z. Magda, X. Jin, I. Hagymási, P. Vancsó, Z. Osváth, P. Nemes-Incze, C. Hwang, L. P. Biró and L. Tapasztó, Room-temperature magnetic order on zigzag edges of narrow graphene nanoribbons, *Nature*, 2014, **514**, 608–611.
2 M. Holicky, B. Fenech-Salerno, A. E. G. Cass and F. Torrisi, Fabrication of graphene field effect transistors on complex non-planar surfaces, *Appl. Phys. Lett.*, 2024, **125**, 113301.
3 W. A. Chalifoux, The Synthesis of Non-planar, Helically Coiled Graphene Nanoribbons, *Angew. Chem., Int. Ed.*, 2017, **56**, 8048–8050.
4 O. El Bakouri, D. W. Szczepanik, K. Jorner, R. Ayub, P. Bultinck, M. Solà and H. Ottosson, Three-Dimensional Fully π-Conjugated Macrocycles: When 3D-Aromatic and When 2D-Aromatic-in-3D?, *J. Am. Chem. Soc.*, 2022, **144**, 8560–8575.
5 M. Baljozović, J. Pijeat, S. Campidelli and K.-H. Ernst, Planar and Curved π-Extended Porphyrins by On-Surface Cyclodehydrogenation, *J. Am. Chem. Soc.*, 2024, **146**, 34600–34608.
6 M. Jurow, A. E. Schuckman, J. D. Batteas and C. M. Drain, Porphyrins as molecular electronic components of functional devices, *Coord. Chem. Rev.*, 2010, **254**, 2297–2310.
7 H. Imahori and S. Fukuzumi, Porphyrin- and Fullerene-Based Molecular Photovoltaic Devices, *Adv. Funct. Mater.*, 2004, **14**, 525–536.
8 R. Paolesse, S. Nardis, D. Monti, M. Stefanelli and C. Di Natale, Porphyrinoids for Chemical Sensor Applications, *Chem. Rev.*, 2017, **117**, 2517–2583.
9 J. M. Park, K.-I. Hong, H. Lee and W.-D. Jang, Bioinspired Applications of Porphyrin Derivatives, *Acc. Chem. Res.*, 2021, **54**, 2249–2260.
10 W. A. Kaplan, K. S. Suslick and R. A. Scott, Core size and flexibility of metallohydroporphyrin macrocycles. Implications for F430 coordination chemistry, *J. Am. Chem. Soc.*, 1991, **113**, 9824–9827.
11 L. T. Scott, M. M. Hashemi and M. S. Bratcher, Corannulene bowl-to-bowl inversion is rapid at room temperature, *J. Am. Chem. Soc.*, 1992, **114**, 1920–1921.
12 H. Huang, T. Stewart, M. Gutmann, T. Ohhara, N. Niimura, Y.-X. Li, J.-F. Wen, R. Bau and H. N. C. Wong, To Flip or Not To Flip? Assessing the Inversion Barrier of the Tetraphenylene Framework with Enantiopure 2,15-Dideuteriotetraphenylene and 2,7-Dimethyltetraphenylene, *J. Org. Chem.*, 2009, **74**, 359–369.
13 I. Ahmad, D. Kim, R. Kodirov, S.-Y. Yu, J.-M. Seo, J. Mahmood and J.-B. Baek, Synthesis of Saddle-Shape

Octaaminotetraphenylene Octahydrochloride, *J. Org. Chem.*, 2021, **86**, 14398–14403.
14 K. Kawasumi, Q. Zhang, Y. Segawa, L. T. Scott and K. Itami, A grossly warped nanographene and the consequences of multiple odd-membered-ring defects, *Nat. Chem.*, 2013, **5**, 739–744.
15 K. Ikemoto, J. Lin, R. Kobayashi, S. Sato and H. Isobe, Fluctuating Carbonaceous Networks with a Persistent Molecular Shape: A Saddle-Shaped Geodesic Framework of 1,3,5-Trisubstituted Benzene (Phenine), *Angew. Chem., Int. Ed.*, 2018, **57**, 8555–8559.
16 K. Ikemoto, D. Nagata, T. Matsuno and H. Isobe, Concise Synthesis of Molecular Hyperboloids by Oligomeric Macrocyclization of Octagonal Molecules, *Chem.–Asian J.*, 2023, **18**, e202300046.
17 E. Solel, D. Pappo, O. Reany, T. Mejuch, R. Gershoni-Poranne, M. Botoshansky, A. Stanger and E. Keinan, Flat corannulene: when a transition state becomes a stable molecule, *Chem. Sci.*, 2020, **11**, 13015–13025.
18 H. Kawashima, N. Fukui, Q. M. Phung, T. Yanai and H. Shinokubo, Planarization of a bowl-shaped molecule by triple-decker stacking, *Cell Rep. Phys. Sci.*, 2022, **3**, 101045.
19 G. J. Bodwell, D. O. Miller and R. J. Vermeij, Nonplanar Aromatic Compounds. 6. [2]Paracyclo[2](2,7)pyrenophane. A Novel Strained Cyclophane and a First Step on the Road to a "Vögtle" Belt, *Org. Lett.*, 2001, **3**, 2093–2096.
20 G. J. Bodwell, J. N. Bridson, M. K. Cyrañski, J. W. J. Kennedy, T. M. Krygowski, M. R. Mannion and D. O. Miller, Nonplanar Aromatic Compounds. 8. 1 Synthesis, Crystal Structures, and Aromaticity Investigations of the 1, n -Dioxa[n](2,7) pyrenophanes. How Does Bending Affect the Cyclic π-Electron Delocalization of the Pyrene System?, *J. Org. Chem.*, 2003, **68**, 2089–2098.
21 A. R. Battersby, D. G. Buckley, S. G. Hartley and M. D. Turnbull, Synthetic studies related to myoglobin: syntheses of bridged porphyrin systems, *J. Chem. Soc. Chem. Commun.*, 1976, 879.
22 Y. Liang, M. Tang and Z. Liu, Molecular Bows—Strained Bow-shaped Macrocycles, *Chem. Lett.*, 2020, **49**, 1329–1336.
23 A. C. Gehrold, T. Bruhn, H. Schneider, U. Radius and G. Bringmann, Monomeric Chiral and Achiral Basket-Handle Porphyrins: Synthesis, Structural Features, and Arrested Tautomerism, *J. Org. Chem.*, 2015, **80**, 12359–12378.
24 A. C. Gehrold, T. Bruhn, H. Schneider, U. Radius and G. Bringmann, Chiral and Achiral Basket-Handle Porphyrins: Short Synthesis and Stereostructures of These Versatile Building Blocks, *Org. Lett.*, 2015, **17**, 210–213.
25 Q. Liu, J. Zhang, M. Tang, Y. Yang, J. Zhang and Z. Zhou, Geometric deconstruction of core and electron activation of a π-system in a series of deformed porphyrins: mimics of heme, *Org. Biomol. Chem.*, 2018, **16**, 7725–7736.
26 Q. Liu, X. Zhang, W. Zeng, J. Wang and Z. Zhou, Fine-Tuning of Electronic Structure of Cobalt(II) Ion in Nonplanar Porphyrins and Tracking of a Cross-Hybrid Stage: Implications for the Distortion of Natural Tetrapyrrole Macrocycles, *J. Phys. Chem. B*, 2015, **119**, 14102–14110.
27 K. Liang, Y. Liang, M. Tang, J. Liu, Z. Tang and Z. Liu, π-Diamond: A Diamondoid Superstructure Driven by π-Interactions, *Angew. Chem., Int. Ed.*, 2024, **63**, e202409507.
28 Y. Dong, L. Qian, F. Chen, Y. Wang, T. Zhang, F. Qiu, T. Teranishi and S. Xue, Benzene-fused porphyrin(2.1.2.1) array: synthesis, structure, and electrocatalytic hydrogen evolution, *Chem. Commun.*, 2024, **60**, 3986–3989.
29 S. Xue, D. Kuzuhara, N. Aratani and H. Yamada, Synthesis of a Porphyrin(2.1.2.1) Nanobelt and Its Ability To Bind Fullerene, *Org. Lett.*, 2019, **21**, 2069–2072.
30 Y. Dong, H. Morimoto, X. Lv, X. Mo, F. Chen, F. Wu, N. Aratani, F. Qiu and S. Xue, Synthesis of Hybrid Porphyrin(2.1.2.1)s and Their Complexation, *J. Org. Chem.*, 2024, **89**, 1626–1632.
31 T. Jiang, Y. Hu, S. Liang, F. Qiu, H. Huang, M. Zhou and S. Xue, Ferrocene unit substitution in nickel(ii) porphyrin(2.1.2.1) induces an extremely low oxygen evolution reaction overpotential, *Dalton Trans.*, 2025, **54**, 8580–8585.
32 S. Xue, W. Ryan Osterloh, X. Lv, N. Liu, Y. Gao, H. Lei, Y. Fang, Z. Sun, P. Mei, D. Kuzuhara, N. Aratani, H. Yamada, R. Cao, K. M. Kadish and F. Qiu, Enhanced Four-Electron Oxygen Reduction Selectivity of Clamp-Shaped Cobalt(II) Porphyrin(2.1.2.1) Complexes, *Angew. Chem., Int. Ed.*, 2023, **62**, e202218567.
33 J. Wu, X. Lv, Z. Xue, Y. Wang, F. Qiu and S. Xue, Metal ions control configuration and $^1O_2$ generation capacity of hexaphyrin(2.1.2.1.2.1) with embedded benzene, *Dalton Trans.*, 2025, **54**, 5255–5258.
34 X. Lv, F. Chen, M. Zhou, T. Zhang, F. Qiu and S. Xue, Synthesis of porphyrin(2.1.2.1) Pd(ii) complexes embedded with various π units and their singlet oxygen generation capacity, *Dalton Trans.*, 2024, **53**, 14433–14437.
35 X. Lv, Y. Dong, J. Wu, T. Jiang, F. Chen, T. Zhang, F. Qiu and S. Xue, Porphyrin(2.1.2.1) organopalladium complexes as efficient singlet oxygen sensitizers, *Dalton Trans.*, 2024, **53**, 5979–5984.
36 S. Xue, N. Liu, P. Mei, D. Kuzuhara, M. Zhou, J. Pan, H. Yamada and F. Qiu, Porphyrin(2.1.2.1) as a novel binucleating ligand: synthesis and molecular structures of mono- and di-rhodium(i) complexes, *Chem. Commun.*, 2021, **57**, 12808–12811.
37 S. Xue, X. Lv, Y. Dong, T. Zhang, F. Qiu, J. Pan, D. Kuzuhara, H. Yamada and N. Aratani, Synthesis of Hetero-Trimetal Porphyrin Nanobelts, *Chem.–Eur. J.*, 2024, **30**, e202402680.
38 S. Xue, Y. Dong, Z. Wang, X. Zhao, T. Zhang, F. Qiu, L. Zhao and J. Pan, Electrocatalytic 4e – Oxygen Reduction through the Innovative Design of a Trinuclear Cobalt Porphyrin(2.1.2.1) Nanobelt, *Inorg. Chem.*, 2024, **63**, 24494–24500.
39 J. H. Zagal, F. Bedioui and J.-P. Dodelet, *N4-Macrocyclic Metal Complexes*, Springer New York, New York, NY, 2006.
40 J. Wu, D. Yoshikawa, D. Kuzuhara, Z. Gao, Y. Wang, H. Huang, F. Qiu and S. Xue, Synthesis and Structure of Porphyrin(2.1.2.1) Bows, *Inorg. Chem.*, 2024, **63**, 24618–24622.

41 Amsterdam Density Functional (ADF 2024) Code, Vrije Universiteit: Amsterdam, The Netherlands, available at: http://www.scm.com.
42 G. Te Velde, F. M. Bickelhaupt, E. J. Baerends, C. Fonseca Guerra, S. J. van Gisbergen, J. G. Snijders and T. Ziegler, Chemistry with ADF, *J. Comput. Chem.*, 2001, **22**, 931–967.
43 M. Ernzerhof and G. E. Scuseria, Assessment of the Perdew–Burke–Ernzerhof exchange-correlation functional, *J. Chem. Phys.*, 1999, **110**, 5029.
44 E. Brémond and C. Adamo, Seeking for parameter-free double-hybrid functionals: The PBE0-DH model, *J. Chem. Phys.*, 2011, **135**, 024106.
45 J. P. Perdew, K. Burke and M. Ernzerhof, Generalized gradient approximation made simple, *Phys. Rev. Lett.*, 1996, **77**, 3865–3868.
46 S. Grimme, Density functional theory with London dispersion corrections, *Wiley Interdiscip. Rev.:Comput. Mol. Sci.*, 2011, **1**, 211–228.
47 G. A. Peralta, M. Seth and T. Ziegler, Magnetic Circular Dichroism of Porphyrins Containing M = Ca, Ni, and Zn. A Computational Study Based on Time-Dependent Density Functional Theory, *Inorg. Chem.*, 2007, **46**, 9111–9125.
48 M. Baranac-Stojanović, New insight into the anisotropic effects in solution-state NMR spectroscopy, *RSC Adv.*, 2014, **4**, 308–321.
49 S. Klod and E. Kleinpeter, Ab initio calculation of the anisotropy effect of multiple bonds and the ring current effect of arenes application in conformational and configurational analysis, *J. Chem. Soc., Perkin Trans. 2*, 2001, **2**, 1893–1898.
50 N. D. Charistos, A. G. Papadopoulos and M. P. Sigalas, Interpretation of Electron Delocalization in Benzene, Cyclobutadiene, and Borazine Based on Visualization of Individual Molecular Orbital Contributions to the Induced Magnetic Field, *J. Phys. Chem. A*, 2014, **118**, 1113–1122.
51 T. Heine, C. Corminboeuf and G. Seifert, The magnetic shielding function of molecules and Pi-electron delocalization, *Chem. Rev.*, 2005, **105**, 3889–3910.
52 R. Islas, T. Heine and G. Merino, The Induced Magnetic Field, *Acc. Chem. Res.*, 2012, **45**, 215–228.
53 T. Ziegler and A. Rauk, A theoretical study of the ethylene-metal bond in complexes between copper(1+), silver(1+), gold(1+), platinum(0) or platinum(2+) and ethylene, based on the Hartree-Fock-Slater transition-state method, *Inorg. Chem.*, 1979, **18**, 1558–1565.
54 M. von Hopffgarten, G. Frenking, M. von Hopffgarten and G. Frenking, Energy decomposition analysis, *Wiley Interdiscip. Rev.:Comput. Mol. Sci.*, 2012, **2**, 43–62.
55 L. Zhao, M. von Hopffgarten, D. M. Andrada and G. Frenking, Energy decomposition analysis, *Wiley Interdiscip. Rev.: Comput. Mol. Sci.*, 2018, **8**, e1345.
56 T. Ziegler and A. Rauk, On the calculation of bonding energies by the Hartree Fock Slater method, *Theor. Chim. Acta*, 1977, **46**, 1–10.
57 J. Moellmann and S. Grimme, DFT-D3 Study of Some Molecular Crystals, *J. Phys. Chem. C*, 2014, **118**, 7615–7621.
58 S. Ehrlich, J. Moellmann and S. Grimme, Dispersion-Corrected Density Functional Theory for Aromatic Interactions in Complex Systems, *Acc. Chem. Res.*, 2013, **46**, 916–926.
59 T. Clark, σ-Holes, *Wiley Interdiscip. Rev.: Comput. Mol. Sci.*, 2013, **3**, 13–20.
60 J. H. Stenlid and T. Brinck, Extending the σ-Hole Concept to Metals: An Electrostatic Interpretation of the Effects of Nanostructure in Gold and Platinum Catalysis, *J. Am. Chem. Soc.*, 2017, **139**, 11012–11015.
61 R. Siddiqui, S. Burguera, M. de las Nieves Piña, S. Dhamija, H. M. Titi, A. Frontera, A. Bauzá and R. Patra, From Coordination to π-Hole Chemistry of Transition Metals: Metalloporphyrins as a Case of Study, *Angew. Chem., Int. Ed.*, 2024, **63**, e202409963.
62 T. Brinck and J. H. Stenlid, The Molecular Surface Property Approach: A Guide to Chemical Interactions in Chemistry, Medicine, and Material Science, *Adv. Theory Simul.*, 2019, **2**, 1800149.
63 L. E. Zelenkov, A. A. Eliseeva, S. V. Baykov, V. V. Suslonov, B. Galmés, A. Frontera, V. Y. Kukushkin, D. M. Ivanov and N. A. Bokach, Electron belt-to-σ-hole switch of noncovalently bound iodine(i) atoms in dithiocarbamate metal complexes, *Inorg. Chem. Front.*, 2021, **8**, 2505–2517.
64 L. E. Zelenkov, A. A. Eliseeva, S. V. Baykov, D. M. Ivanov, A. I. Sumina, R. M. Gomila, A. Frontera, V. Y. Kukushkin and N. A. Bokach, Inorganic–organic $\{dz^2\text{-}M^{II}S_4\}\cdots\pi$-hole stacking in reverse sandwich structures: the case of cocrystals of group 10 metal dithiocarbamates with electron-deficient arenes, *Inorg. Chem. Front.*, 2022, **9**, 2869–2879.
65 Z. M. Bikbaeva, D. M. Ivanov, A. S. Novikov, I. V. Ananyev, N. A. Bokach and V. Y. Kukushkin, Electrophilic–Nucleophilic Dualism of Nickel(II) toward Ni···I Noncovalent Interactions: Semicoordination of Iodine Centers *via* Electron Belt and Halogen Bonding *via* σ-Hole, *Inorg. Chem.*, 2017, **56**, 13562–13578.
66 H. Böhrer, N. Trapp, D. Himmel, M. Schleep and I. Krossing, From unsuccessful H 2 -activation with FLPs containing B(Ohfip) 3 to a systematic evaluation of the Lewis acidity of 33 Lewis acids based on fluoride, chloride, hydride and methyl ion affinities, *Dalton Trans.*, 2015, **44**, 7489–7499.
67 T. E. Mallouk, G. L. Rosenthal, G. Mueller, R. Brusasco and N. Bartlett, Fluoride ion affinities of germanium tetrafluoride and boron trifluoride from thermodynamic and structural data for (SF3)2GeF6, ClO2GeF5, and ClO2BF4, *Inorg. Chem.*, 1984, **23**, 3167–3173.
68 M. Lehmann, S. N. Balogun, M. Reimann and M. Kaupp, The Fluoride Ion Affinity Revisited: Do We Need the Anchor-Point Approach?, *Chem.–Eur. J.*, 2025, **31**, e202404662.
69 X. Guo, F. Unglaube, U. Kragl and E. Mejía, $B(C_6F_5)_3$-Catalyzed transfer hydrogenation of esters and organic carbonates towards alcohols with ammonia borane, *Chem. Commun.*, 2022, **58**, 6144–6147.
70 R. Scott, D. Shriver and D. Lehman, The lewis basicity of metal complexes. BF3 and (C6F5)3 adducts of

IrClCO(O(C6H5)3)2 and related systems, *Inorg. Chim. Acta*, 1970, **4**, 73–78.
71 H. Frohn, in *Efficient Preparations of Fluorine Compounds*, Wiley, 2012, vol. 4, pp. 60–64.
72 J. R. Gaffen, J. N. Bentley, L. C. Torres, C. Chu, T. Baumgartner and C. B. Caputo, A Simple and Effective Method of Determining Lewis Acidity by Using Fluorescence, *Chem*, 2019, **5**, 1567–1583.
73 P. Erdmann, J. Leitner, J. Schwarz and L. Greb, An Extensive Set of Accurate Fluoride Ion Affinities for p -Block Element Lewis Acids and Basic Design Principles for Strong Fluoride Ion Acceptors, *ChemPhysChem*, 2020, **21**, 987–994.
74 G. Merino, T. Heine and G. Seifert, The Induced Magnetic Field in Cyclic Molecules, *Chem.–Eur. J.*, 2004, **10**, 4367–4371.